




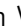




Severe atmospheric pollution in the Middle East is attributable to anthropogenic sources

Sergey Osipov ¹, Sourangsu Chowdhury ¹, John N. Crowley¹, Ivan Tadic ¹, Frank Drewnick², Stephan Borrmann ², Philipp Eger¹, Friederike Fachinger², Horst Fischer¹, Evgeniya Predybaylo¹, Mohammed Fnais³, Hartwig Harder¹, Michael Pikridas⁴, Panos Vouterakos⁴, Andrea Pozzer ¹, Jean Sciare⁴, Alexander Ukhov⁵, Georgiy L. Stenchikov ⁵, Jonathan Williams ¹ & Jos Lelieveld ^{1,4✉}

In the Middle East, desert dust is assumed to dominate air pollution, being in permanent violation of public health guidelines. Here we present ship-borne measurements from around the Arabian Peninsula and modeling results to show that hazardous fine particulate matter is to a large extent of anthropogenic origin (>90%), and distinct from the less harmful, coarse desert dust particles. Conventionally, it was understood that desert dust dominates both the fine and coarse aerosol size fractions, which obscures the anthropogenic signal. We find that the annual excess mortality from the exposure to air pollution is 745 (514-1097) per 100,000 per year, similar to that of other leading health risk factors, like high cholesterol and tobacco smoking. Furthermore, anthropogenic pollution particles account for a major part (~53%) of the visible aerosol optical depth. Therefore, in the Middle East anthropogenic air pollution is a leading health risk and an important climatic factor.

¹ Atmospheric Chemistry Department, Max Planck Institute for Chemistry, 55128 Mainz, Germany. ² Particle Chemistry Department, Max Planck Institute for Chemistry, Mainz, Germany. ³ King Saud University, College of Science, Riyadh 11451, Saudi Arabia. ⁴ Atmosphere and Climate Research Center, The Cyprus Institute, 2121 Aglantzia, Cyprus. ⁵ King Abdullah University of Science and Technology, Thuwal 23955-6900, Saudi Arabia. ✉email: jos.lelieveld@mpic.de

The climate and air quality of the Middle East have been defined by natural drivers, such as the large-scale atmospheric circulation, the presence of deserts and airborne dust^{1–3}. The descending branch of the Hadley cell brings with it adiabatically heated and dry air and determines the location of the Earth's hot deserts, including the vast African Sahara and Arabian Empty Quarters. The Middle East is located in the “dust belt”, and on average experiences twenty major dust storms per year⁴. Boosted by the lack of precipitation, the elevated mineral dust concentrations have a profound effect on ecosystems, human activity, and influence the climate by interacting with solar and terrestrial radiation. By exerting a strong radiative forcing, dust modulates the planetary energy balance and alters the heat budget of the seas⁵. Over the southern Red Sea, it generates the world's largest solar radiative cooling reaching 60 W/m^2 ⁶.

The human footprint of the Middle East, with a population of about 400 million, is evident as the region emits more than 15% of the global SO_2 pollution and $\sim 7.5\%$ of the greenhouse gases^{7–9}. Several studies have addressed the air quality in the Middle East, indicating that a large fraction of the pollution is unaccounted for in emission inventories^{10–12}. Poor representation of emissions, together with the lack of observational data, constitute a considerable modeling challenge and hinder our understanding of the atmospheric composition in the region. Therefore, the shipborne measurement campaign AQABA (Air Quality and climate in the Arabian Basin) was conducted in the summer of 2017 (Fig. 1, Supplementary Fig. S1)^{13–17}. For two months, numerous instruments characterized the atmospheric chemistry around the Arabian Peninsula as well as the influence of emissions in the wider area of the Middle East (Supplementary Table S1). The observations covered various ambient conditions that ranged from pristine in the remote atmosphere to heavy pollution and dust storms.

Here, we employ the AQABA observations to characterize the ambient air pollution and test simulations with a regional chemistry-transport model. First, we discuss the ozone (O_3) chemistry and then the particulate matter (PM) observed in the boundary layer, making a distinction between “fine” and “coarse” aerosols. We define the fine PM as the sum of particles in the Aitken and accumulation size modes up to $1 \mu\text{m}$ in diameter, which also covers a large part of the size range up to $2.5 \mu\text{m}$ ($\text{PM}_{2.5}$) used in air quality assessments. Taking the submicron

PM fraction allows a direct comparison between the field observations and model results. While the fine aerosol mode constitutes only a small mass fraction relative to the coarse mode, it dominates the number concentration which is relevant for human health and the scattering of sunlight.

Results

Photochemical ozone pollution. Figure 2 presents model results that illustrate the exceptional pollution levels in the Middle East. The conditions contributing to high ozone levels in the Middle East have been studied previously^{10,11,15}. Any model that aims to successfully simulate tropospheric O_3 in the Middle East must incorporate stratosphere-troposphere exchange, long-distance transport and indigenous emissions. According to ref. ¹⁰, the unusually strong stratosphere-troposphere exchange over the Middle East contributes up to 25% of the tropospheric ozone column in summer. The long-distance transport of air pollution via the Mediterranean fosters the local O_3 photochemistry since the region is influenced by European emissions, but also from North America and Asia^{18,19}. During summer, eastern European sources contribute most significantly to the transport. In addition to advection and vertical entrainment, O_3 formation in the boundary layer is particularly strong due to indigenous industrial and urban activities that cause emissions of nitrogen oxides ($\text{NO}_x = \text{NO} + \text{NO}_2$) and reactive volatile organic compounds (VOC).

The AQABA observations confirm these previous findings and reveal several novel features. Supplementary Fig. S4 shows that the Gulf of Suez, the northern Red Sea and especially the Arabian Gulf stand out as the regional ozone hot spots. Net O_3 production in these regions is exceedingly high (up to 32 ppbv day^{-1} , according to ref. ¹⁵), making them the main “exporters” of ozone in the Middle East. During the AQABA campaign, the ship was twice stationary at Jeddah and Kuwait, which allowed a focus on finer scales. Measurements made during these stops, and reproduced by our model, reveal the lowest levels of ozone and resolve the diel cycle of the meteorology (land-sea breezes), photochemistry and emissions. Supplementary Fig. S4 shows the O_3 titration events taking place in proximity of the large NO emission point sources. Overnight ozone depletion through reaction with NO is reflected in the NO_2 levels, which are elevated at least by an order of magnitude.

Over the Arabian Gulf, the model does not capture the ozone variability above 80 ppbv. We find that net O_3 production and organic peroxy radicals (RO_2) exhibit similarly erratic fluctuations, suggesting that the elevated levels of ozone are due to exceptionally strong local formation. Oxidation of VOC from the petrochemical industry (given the absence of natural sources) could explain the elevated RO_2 and O_3 variability. According to backward trajectory analysis (Supplementary Fig. S14), the ozone-rich air masses originated and chemically aged over a narrow strip of the densely populated and industrialized Mesopotamia region (the Tigris-Euphrates Basin). The corresponding sources in Mesopotamia are likely to be missing or misplaced in the emission inventory, as regional anthropogenic sources are notoriously underestimated^{7,20,21}.

We emphasize the extent of the long-term exposure to O_3 and NO_2 in the region. Figure 2a, b illustrates that the mean ozone levels in July and August top the WHO seasonal guideline mixing ratio of $\sim 30 \text{ ppbv}$, and the daily maximum 8-hourly O_3 exceeds the 50 ppbv limit²². Modeled NO_2 pollution is more confined spatially, but also significantly exceeds the WHO guideline of $10 \mu\text{g m}^{-3}$ ($\sim 5.5 \text{ ppbv}$ assuming standard temperature and pressure) over the populated regions in the Middle East. According to ref. ¹⁵, the net ozone production in the Middle



Fig. 1 Ship measurement track of the AQABA campaign. Ship track (two-way, light blue line) from late June to early September 2017. Red circles indicate two stops at Jeddah and Kuwait. The meteorology during summer, characterized by a heat low over the Arabian Peninsula, brings about a wide range of pollution conditions along the track. Prevailing wind directions are indicated by the arrows.

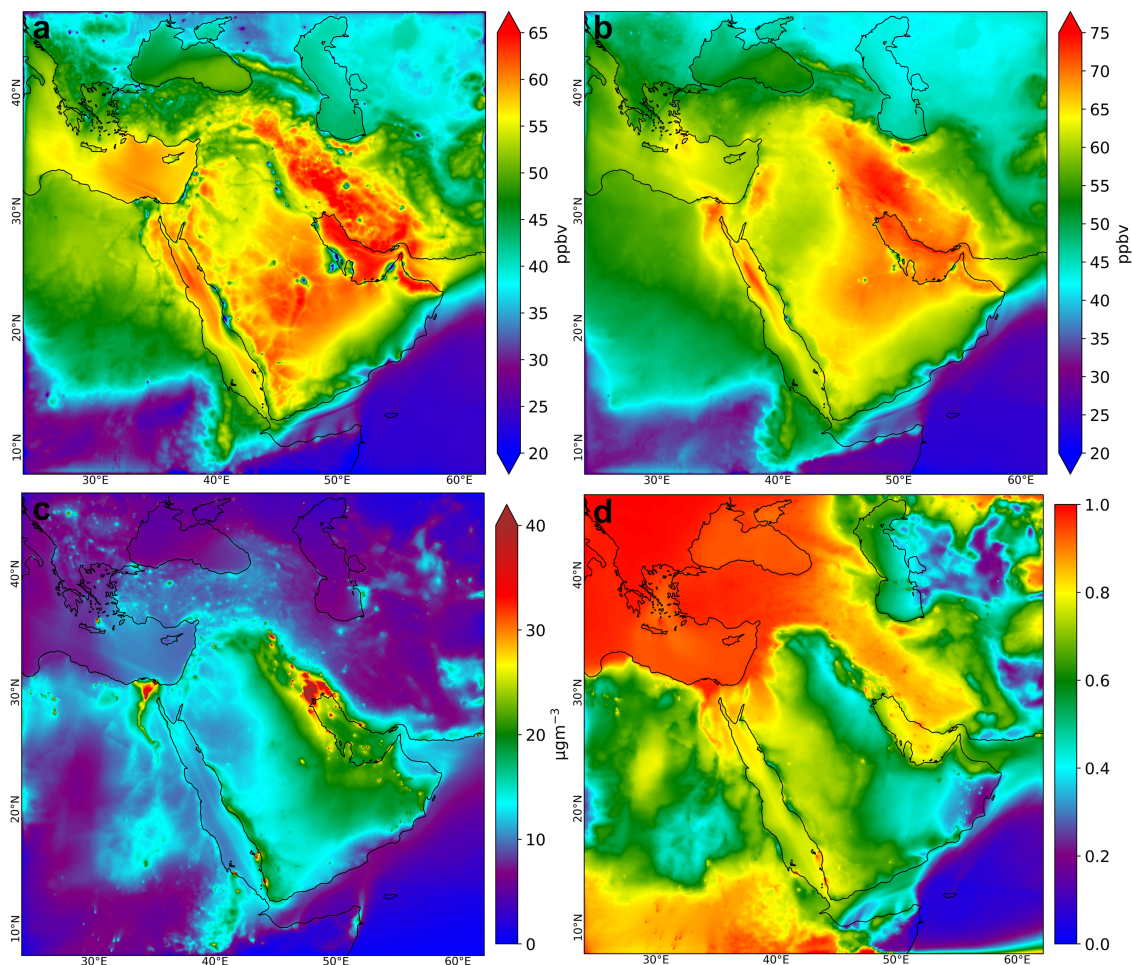


Fig. 2 Model results for ozone and fine particulate matter. **a** Mean O_3 at the surface (ppbv), **b** daily maximum 8-hourly O_3 (ppbv), **c** fine, submicron PM ($\mu\text{g m}^{-3}$), **d** anthropogenic fraction of fine PM (dominated by ammonium, sulfate, nitrate, black and organic carbon). The biogenic emissions were assumed to be negligible in the region and are not included in the simulation. Figure represents the average of the July–August 2017. Biomass burning is considered anthropogenic.

East is mostly NO_x -limited or happens in the transition regime between NO_x and VOC limitation. This implies that NO_x reduction would be an effective O_3 mitigation measure in the Middle East, while VOC reduction is also a viable strategy in the Mediterranean, northern Red Sea and Gulf of Oman regions, where a transition regime is found.

Aerosol pollution and attribution. To characterize the aerosol particles in detail, we have employed several collocated measurement techniques. A suite of instruments was used to measure the aerosol size distribution from 5 nm to 32 μm (Table S1). The size distribution does not contain information about individual aerosol species but can be integrated to yield the total concentrations of aerosols of a certain size (e.g. PM_{10}). We derived the dry aerosol composition from the aerosol mass spectrometer (AMS), aethalometer and ion chromatography (IC) measurements. These instruments detect specific aerosol components and measure the bulk concentrations. The AMS detected the non-refractory particles (sulfate, ammonium, nitrate and total organics) within the fine aerosol fraction (PM_{10}). The aethalometer complemented the PM_{10} composition with the black carbon (BC) concentrations. Together, the AMS and aethalometer cover only the fine fraction. To achieve closure, we incorporated the natural aerosols (sea salt and dust) from the IC measurements (Fig. 3). Supplementary Fig. S5 presents the organic aerosol (OA) fraction.

Figure 3 presents the observed chemical composition of the fine aerosol. The total non-specified fine PM is in agreement with the sum of the specified components for most of the campaign, indicating that OA, SO_4^{2-} , NH_4^+ , and BC constitute the bulk of the fine aerosol by mass, which is supported by our model results. Thus, the fine PM fraction in the boundary layer is almost entirely anthropogenic and natural aerosols (dust and sea salt) make only a minor and infrequent contribution. Organic aerosols are prominent in the northern part of the region, i.e. over the Mediterranean Sea, Gulf of Suez and northern Red Sea, and represent 40% (median value) of the fine PM measured during the campaign (Fig. 3). Ammonium sulfate contributes considerably 61% (median value) throughout the area. Over the Arabian Gulf, ammonium sulfate produces the highest levels of fine aerosol pollution, reaching 30–50 $\mu\text{g m}^{-3}$. Water is an important component of the aerosol in this humid area (observed relative humidity is shown in Supplementary Fig. S13). BC concentrations are not uniform spatially and exhibit sharp spikes in the proximity of urban and industrial pollution centers.

The Middle East is a major global SO_2 emission hotspot, mostly from fossil energy production and the petrochemical industry^{7,8}. Strong SO_2 point sources constitute a large fraction¹¹, and these are included in our model based on satellite measurements. Due to intense marine traffic, ship emissions contribute to the sulfate pollution and dominate the background sulfate concentrations in remote and pristine areas (Supplementary Fig. S6). Supplementary

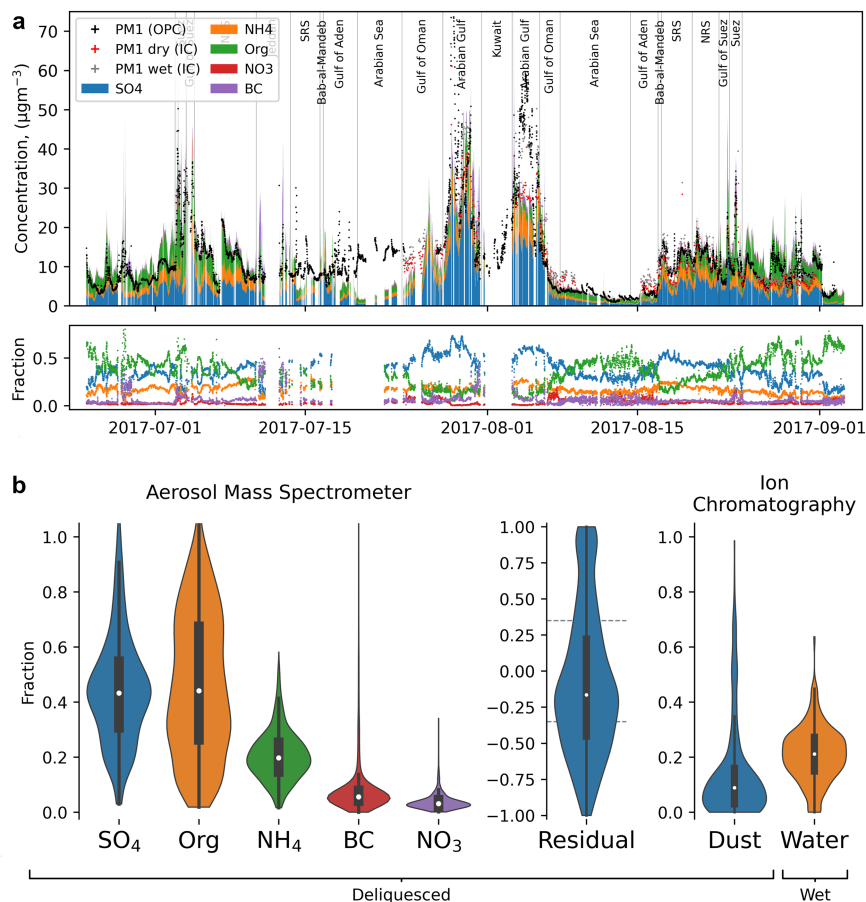


Fig. 3 Fine aerosol composition during the AQABA campaign. **a** The stacked area plot shows the five major components (sulfate SO_4^{2-} , ammonium NH_4^+ , total organics Org, nitrate NO_3^- , black carbon BC) of the deliquesced (40% RH) particles measured by the aerosol mass spectrometer (AMS) and aethalometer. Black dots indicate the total non-speciated aerosol obtained by integrating the size distribution (OPC). Red and gray dots indicate the speciated aerosol measured by ion chromatography (IC). These measurements include the contributions from dust and sea salt, but not ammonium. Red dots indicate the sum of the dry particle components. Gray dots include the aerosol water, calculated with an aerosol thermodynamics model³⁵. **b** Violin plots show the summary statistics, with the median, interquartile range and kernel density of the speciated fine PM fractions relative to the total non-speciated fine PM, with a residual of ~15%.

Fig. S6 shows that most of the time simulations capture the SO_2 spatial gradients between remote and polluted atmospheres without an evident bias, albeit with a few exceptions, related to nearby ship emissions. Observations reveal strong subhourly SO_2 variability, which is adequately represented by our model given the daily resolution of the marine traffic emissions. However, simulations do not capture the distinct SO_2 spikes between the Bab-al-Mandeb Strait and the Gulf of Oman, which are likely due to nearby ship emissions, not adequately represented by our model. The absence of similar variability in the sulfate concentrations also points to fresh pollution emissions. We note the immensely high SO_2 mixing ratios in excess of 100 ppbv close to the Gulf of Suez, Jeddah and Kuwait.

In the aerosol phase, sulfur is much more spatially uniform than in the gas phase. Simulated sulfate concentrations are in close agreement with observations for all regions apart from the Arabian Gulf (Supplementary Fig. S6). In this region, the model underestimates the heavy sulfate pollution. This low bias could be due to sulfate emissions directly in the aerosol phase or to an unaccounted for rapid SO_2 oxidation pathway. Among possible mechanisms explaining the accelerated SO_2 oxidation is the ozonolysis of alkenes producing Criegee intermediates²³ and liquid phase oxidation²⁴. The necessary conditions for these phenomena, including elevated ozone, reactive VOC and high aerosol water concentrations, are met in the Arabian Gulf region.

Acidification accounts for many of the deleterious effects that air pollution exerts on ecosystems. Our simulations reveal (Supplementary Fig. S16) that coastal regions are most intensely exposed to sulfur deposition, with the Red Sea, Arabian Gulf and the adjacent coasts of the Arabian Peninsula, as well as the Eastern Mediterranean area particularly affected. It is critical that the deleterious effects of “acid rain” be considered, especially in ambitious projects such as the Green Middle East and Saudi initiatives, whose aims include the planting of 40 billion trees in the region.

Total ammonia ($\text{NH}_x = \text{NH}_3 + \text{NH}_4^+$) partitions between the gas and particle phase and, by definition, $\text{NH}_x \geq \text{NH}_4^+$. AQABA observations confirm that a significant amount of ammonium is present in the region (Supplementary Fig. S7), but the precursor NH_3 was not measured. Focusing on total ammonia NH_x , we show that NH_3 emissions in the Middle East are severely underestimated, likely by more than a factor of 15. Natural sources of ammonia are negligible in the Middle East with the vast majority originating from industrial and agricultural activities. Supplementary Fig. S7 demonstrates that the EDGAR emission inventory used in our model underestimates the NH_3 emissions and cannot explain the observed ammonium concentrations. Simulations, coupled to the original EDGAR emissions, result in NH_x concentrations (both in gas and particle phases) that are at least an order of magnitude smaller than those measured in PM_{10} . This result is consistent with the conclusions of

van Damme et al.²⁰, who pointed out that NH₃ point sources in EDGAR are typically underestimated by an order of magnitude, while area sources are in agreement with the satellite-derived emission fluxes within a factor of three or larger. Our sensitivity analysis shows that satellite-derived point sources of NH₃ alone (i.e. from van Damme et al.²⁰) are not sufficient to establish a realistic background, indicating that area sources play a major role. Supplementary Fig. S7 shows that increasing the agricultural emissions (being the main source) 15 times leads to approximately realistic model results, capturing the bulk of the ammonium variability in the background and polluted atmospheres. Thus, ammonia emission estimates are particularly uncertain and represent the principal challenge in modeling reactive nitrogen in the Middle East.

Particulate BC is the product of incomplete combustion of biomass and fossil fuels. It is a potent, short-lived climate forcer^{25,26} and toxic air pollutant²⁷. Supplementary Figs. S8 and S9 show that observed BC concentrations span three orders of magnitude from 10⁻² μg m⁻³ to >10 μg m⁻³. The lowest concentrations were measured over the Arabian Sea, where the air masses are pristine under the influence of the Somali jet. Over the seas surrounding the Arabian Peninsula the BC pollution is relatively pronounced due to active shipping with background concentrations of up to 1 μg m⁻³. BC concentrations exceed 10 μg m⁻³ near the urban and industrial pollution centers, for example Suez, the port of Jeddah and the Arabian Gulf. Such concentrations of BC are regarded as particularly hazardous to human health²⁷.

Supplementary Fig. S8 shows that the speciated black carbon (BC) emissions alone cannot explain the observed BC concentrations. Simulations, coupled to such emissions, underestimate the BC concentrations by a factor of 2–3 in the Middle East in general and by 1–2 orders of magnitude over the Arabian Gulf specifically. The substantial underestimation of BC in the Middle East is in line with global modeling studies, which similarly concluded that the BC emission inventories are not representative of the true conditions. We were able to remedy this problem by considering the total PM_{2.5} emissions reported by the inventories.

The EDGARv5.0, Wiedinmyer and GFASv12 inventories provide the BC, OC and the bulk PM_{2.5} (which includes BC and OC) emissions separately. The remainder of the total and speciated emissions (UPM_{2.5}) is non-speciated and equals PM_{2.5}–BC–OC. Supplementary Fig. S8 shows that the inclusion of the UPM_{2.5} as BC allows the realistic simulation of the background concentrations and removal of the bias across all pollution regimes apart from the underestimated heavy pollution over the Arabian Gulf. We note that the non-speciated component of the PM_{2.5} emissions is often discarded in modeling studies and this omission could partially explain the low simulated concentrations of BC globally²⁸. We recommend to also test this assumption for other geographical regions of the world.

Supplementary Fig. S3 summarizes the model skill to simulate the anthropogenic part of the air pollution (trace gases and fine particulate matter) and presents scatter plots that compare measurements with model results, detailed in subsequent figures. Supplementary Fig. S4 shows that our simulations generally capture the O₃ and NO₂ levels both in the polluted and remote (i.e. Arabian Sea) atmospheres, suggesting that meteorology, ozone-related emissions and chemistry are represented well (except over the Arabian Gulf—discussed below). The comparison at the ports of Jeddah and Kuwait confirms the model's suitability for representing the discrete effects of emissions from local sources. For completeness, in Supplementary Fig. S13 we compare the modeled with measured meteorological data. In the next sections we focus on the air pollution of natural origin, and add observational constraints to further evaluate the model and characterize the aerosol optical properties in the Middle East.

Role of mineral dust. Mineral dust is the most abundant aerosol by mass overall and is generated by winds over dry and bare soils. The emission mechanism is complex and involves fine-scale geophysical processes, which are typically not resolved by atmospheric and climate models. Instead, the emission flux in the models is conventionally parameterized based on empirical relations and then tuned²⁹. We employed the AQABA observations (i.e., aerosol optical properties, coarse and fine PM) to optimize the dust mass flux into the atmosphere (Supplementary Fig. S10) and show that simulations realistically represent the size distribution, life cycle and mass balance of dust.

The partitioning of the aerosol optical properties is consistent with the chemical composition and the size distribution of the aerosols, which in first approximation define the aerosol optical depth (AOD). Above we have constrained the fine aerosol fraction and showed that the entire accumulation mode is primarily anthropogenic by mass. For dust, this implies that the accumulation mode of the emitted size distribution is not required and, thus, the emission scheme only needs to account for the coarse mode. In Supplementary Fig. S11 we compare our particular unimodal size distribution of the emitted dust with the general bimodal case. We note that the single empirical mode conceptually and quantitatively agrees well with the theoretical size distribution³⁰ that originates from the fragmentation of the brittle material.

We impose further constraints on the simulated dust size distribution and employ ion chromatography (IC) observations of the ambient fine mode and total PM. According to the IC data, fine mode dust PM concentrations in the boundary layer are about 1–3 μg m⁻³. By integrating the left tail of the size distribution up to 1 μm, we obtain similar concentrations in our model simulations. The concentrations of the coarser dust particles were also measured by IC (Supplementary Fig. S12) and mostly span the range of 10–10² μg m⁻³ with much higher temporal variability than the fine PM. These measurements, however, underestimate the total coarse PM dust concentrations due to transmission loss (Supplementary Fig. S2), which inevitably occurs in the inlet due to a number of reasons (e.g. inertial deposition, sedimentation). We estimate that the loss reaches 8% for particles with aerodynamic diameters of 5 μm, 60% for 10 μm and 99% for 15 μm (i.e. spectral loss function). To compare the observed and simulated ambient concentrations of the coarse dust, we accounted for the effect of the transmission loss and weighted the simulated size distribution using the spectral loss function. Supplementary Fig. S12 shows that our dust simulations exhibit a variability which is similar to that of the IC data and predict dust concentrations across scales without significant bias.

Our results suggest that in the Middle East anthropogenic and natural particles represent different parts of the modal aerosol distribution with respect to size and optical properties. Anthropogenic components govern the accumulation mode, while natural aerosols, notably airborne dust particles, are confined to the coarse mode. One exception may be nitric acid, which can partition to the dust particles and react with cations to form nitrate³¹. This implies that a small fraction of the coarse mode aerosol should be attributed to anthropogenic NO_x sources. Accounting for the accumulation mode of the emitted dust size distribution appears to be redundant and produces diagnostics (PM categories, column AOD) inconsistent with observations. On the other hand, the unimodal (coarse) size distribution of the emitted dust is consistent with the scaling theory derived from first principles. The previously underrated human-caused pollution emissions may have been associated with the inclusion of dust in the accumulation mode in models and satellite retrieval algorithms.

Aerosol optical properties. Related to the paucity of observations and limited knowledge about the chemical composition of PM in the Middle East, the AOD is often assumed to be determined primarily by dust. Supplementary Figs. S10–S12, however, reveal that during the AQABA campaign the accumulation mode of the size distribution, being anthropogenic, explains more than half (53%, median value) of the total AOD at 500 nm wavelength, thus equivalent to the natural coarse aerosol component. In polluted air, especially over the northern Red Sea area and near the Gulf of Suez, the anthropogenic fraction accounts for 80–95% of the AOD and almost completely explains the AOD variability. The remainder of the column AOD is mostly accounted for by dust.

Since the natural (coarse) and anthropogenic (fine) components are distinct by size, we employed the Angstrom exponent (AE) to further analyze the aerosol partitioning and to constrain the spectral dependence of the aerosol optical properties on the wavelength. Supplementary Fig. S10 shows that simulations capture the elevated AE values close to the polluted areas (indicating the prevalence of fine anthropogenic aerosols) and lower AE values in the dusty regions. It follows that the direct radiative effects on climate by aerosol particles in the Middle East is significantly related to anthropogenic pollution, and on average of similar magnitude as that of the abundant airborne desert dust.

Concluding the AQABA data analysis and model validation, we note that the observations were obtained during a single season and year. Continued measurements will be needed to test the model skill in capturing the seasonal and multi-year variability, by also accounting for the temporal emission profiles.

Air pollution health burden. By considering the $5\ \mu\text{g m}^{-3}$ (annual mean) and $15\ \mu\text{g m}^{-3}$ (24-hour mean) thresholds recommended by the WHO for $\text{PM}_{2.5}$, it is clear that the health guideline concentrations are permanently exceeded by a large margin in the Middle East (Fig. 4). After testing the model for the AQABA period, we simulated the annual exposure to air pollution to estimate the health impacts. We calculated the excess mortality burden, following the recently updated methodology according to the Global Burden of Disease (GBD) studies^{32–35}. Supplementary Table 1 presents the country-level exposure to $\text{PM}_{2.5}$ and the excess mortality attributed to air pollution, being dominated by $\text{PM}_{2.5}$ (89% region-wise) over O_3 . The excess mortality due to $\text{PM}_{2.5}$ in the Middle East ranges between 5.9% (Cyprus) and 15.9% (Kuwait). Comparison with the USA and Germany, where the corresponding figures are 3.0% and 3.7%³⁴, respectively, underscores the challenging air quality conditions in the Middle East.

Our results are consistent with the GBD assessment³³, which attributes 12.9% (11.6–14.0%) of mortality in the Middle East to air pollution. According to the GBD database, the health risk of exposure to air pollution in the region is similar to that of high LDL (low-density lipoprotein) cholesterol (13.2%) and tobacco use (14.0%, including smoking, chewing tobacco, and secondhand smoke) risks. To put the magnitude of the air pollution health outcome in the Middle East further into perspective, we report the annual mortality due to COVID-19 (calculated from the period 17 November 2019 to 4 September 2021, <https://www.statista.com>). Although not directly compatible (one being a health risk and the other a disease), the annual excess mortality attributable to poor air quality (11.5% due to $\text{PM}_{2.5}$ and O_3) and that from COVID-19 (7.6% region-wise and 10.3% excluding Egypt, Syria and Yemen as low-outliers) are similar, but noting that the health impacts from air pollution are of long-term duration.

While the submicron PM is almost entirely anthropogenic, about half of the $\text{PM}_{2.5}$ is desert dust (52% region-wise, thus including scarcely populated deserts). Nevertheless, a large part of the health hazardous $\text{PM}_{2.5}$ (above the WHO guideline) is anthropogenic and avoidable, while this fraction is higher in populated areas due to the vicinity of anthropogenic sources. For O_3 the unhealthy levels are entirely anthropogenic. For several countries (Kuwait, Egypt, Bahrain, Iraq, Oman, Saudi Arabia), the adverse health effects of air pollution (natural and anthropogenic) are particularly severe. Since anthropogenic emissions constitute a major fraction of $\text{PM}_{2.5}$ and O_3 , they represent an obvious target for improving air quality in the Middle East. Specific recommendations on air quality and how it can be improved can be found in the WHO guidelines¹⁹.

Conclusions

A unique combination of pollutants present at abundant concentrations distinguishes ambient air pollution in the Middle East from other areas of the world. Until now, air quality in the Middle East was considered to be primarily affected by the vast amounts of natural dust. The AQABA observations and model results reveal that this view is incorrect and that anthropogenic emissions are inherent and prominent. We find that anthropogenic and natural aerosols are mostly segregated in size and optical properties. Anthropogenic aerosols dominate the ambient particle number concentration and explain more than 50% of the column AOD (in the visible spectrum). This demonstrates that human-caused particulate matter induces a radiative forcing equivalent to the abundant natural dust. Since aerosols are a major driver of climate and health impacts in the Middle East, the anthropogenic component should be adequately represented in assessments of air quality and climate change.

Methods

Regional chemistry-transport modeling. The Weather Research and Forecasting-Chem (WRF-Chem) model integrates atmospheric chemistry, aerosol processes and meteorology and their interactions at every time step^{36,37}. We configured WRF-Chem to simulate the tropospheric chemistry in the Middle East, for the domain $6.67^\circ\text{--}45.56^\circ\text{N}$ and $22.92^\circ\text{--}69.66^\circ\text{E}$ at a spatial resolution of 10 km. We used the Earth System Research Laboratory (ESRL) version of the Regional Atmospheric Chemistry Mechanism (RACM) to simulate gas phase chemistry^{38,39} and used a modal approach, namely the Modal Aerosol Dynamics model for Europe (MADE), to simulate aerosols⁴⁰ and ISORROPIA-II for thermodynamic processes⁴¹. The Volatility Basis Set (VBS) mechanism was applied to simulate the secondary organic aerosol (SOA) formation and chemical aging. To resolve the long-range transport of important air pollutants originating outside of the modeling domain, we imposed initial and boundary conditions. We prescribed several trace gases (O_3 , SO_2 , CO) and aerosols (sulfate, organic and black carbon, dust, sea salt) from the Modern-Era Retrospective analysis for Research and Applications, Version 2 (MERRA-2)⁴².

We applied a mixing ratio of CH_4 at 1.8 ppmv throughout the domain for boundary conditions to account for the major sink of OH radicals. To include sources of pollution located within the modeling domain, we prepared the anthropogenic emissions using the HERMESv3 framework⁴³ and several emission inventories: CAMS-GLOB-SHIPv2.1 (shipping emissions, including VOC)⁴⁴, HTAPv2 (only VOC, excluding shipping)⁴⁵, OMI-HTAPv2 (only SO_2)²¹, EDGARv5 (all air pollutants excluding shipping emissions, VOC and industrial SO_2 from the energy industry, combustion for manufacturing, oil refineries and transformation industry)⁴⁶, waste burning⁴⁷, GFASv12 for biomass burning⁴⁸, natural alkene emissions from the Red Sea¹⁴, sources of NH_3 ²⁰ and BC point sources from flaring⁴⁸. Finally, we accounted for the intrinsic diurnal and weekly cycles of anthropogenic emissions (such as traffic rush hours and weekends), noting that the weekend days in the Middle East are Friday and Saturday. A visualization of the modeled meteorology and main aerosol types can be found here: <https://www.youtube.com/watch?v=KF12n3glxjU>. It also illustrates how air pollution from the Middle East is entrained into the Somali jet, providing a transport pathway to South Asia⁴⁹. The biogenic emissions were assumed to be negligible in the region and are not included in the simulation.

Unaccounted anthropogenic emissions. Above we demonstrated that, in particular over the region of the Arabian Gulf, the model consistently underestimates the concentration of a number of air pollutants, while performing well

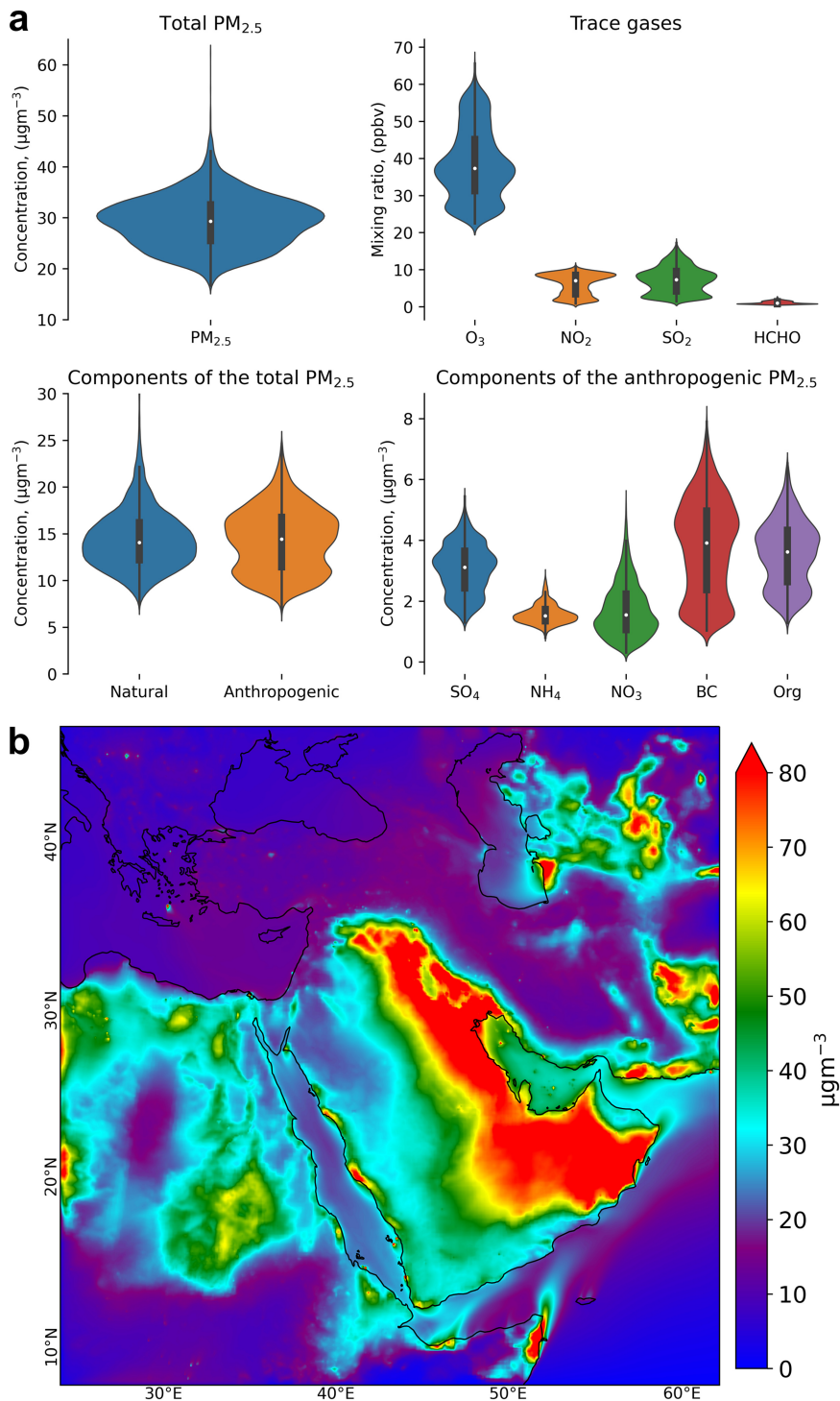


Fig. 4 Model calculated air pollution in the Middle East. a Violin plots show the population weighted PM_{2.5} and trace gases, the natural and anthropogenic components of PM_{2.5}, and the composition of anthropogenic PM_{2.5}. Natural PM_{2.5} is largely due to dust. **b** Spatial distribution of the total PM_{2.5} (not population weighted, $\mu\text{g m}^{-3}$), showing that the WHO guideline concentration of $5 \mu\text{g m}^{-3}$ is exceeded everywhere except over the Arabian Sea, and that ambient PM_{2.5} concentrations can be exceptionally high. The five major aerosol components are sulfate SO_4^{2-} , ammonium NH_4^+ , total organics Org, nitrate NO_3^- , black carbon BC.

elsewhere in the Middle East and across different regimes of pollution. This is a strong indication that a specific source category of emissions is missing in the inventories. According to backward trajectory analysis (Supplementary Fig. S14), prior to arriving in the Arabian Gulf area, the air masses originated and aged over a narrow strip above the populated and industrialized Mesopotamia region (Tigris-Euphrates Basin). Here, we elaborate arguments that trace the missing source of emissions to the petroleum industry concentrated in this region.

According to McLinden et al.⁷, multiple strong SO_2 and NO_2 point sources (originating from flaring activity) in the Middle East are not represented in the conventional emission inventories. We extended this notion and tested the hypothesis that the inventories do not account for combustion products from flaring activity in general (i.e., BC, sulfate and VOC). Our aethalometer measurements of absorbing aerosols confirm the “fossil fuel” signature of the missing BC source. Using spectral absorption measurements, we estimated the ratio of the “fossil fuel” and “biomass burning” related BC⁵⁰ (Supplementary

Table 1 Annual mean exposure, total death rate and excess mortality (with the 95% confidence intervals in parentheses).

Country	PM _{2.5} * (µg/m ³)		Death rate (/100,000/yr)	Excess mortality (/100,000/yr)		Excess mortality (%)	
	Total	Anthropogenic		PM _{2.5}	O ₃	PM _{2.5}	O ₃
Middle East	37.4	17.8	6440 (5710-7301)	666 (460-982)	79 (54-115)	10.3	1.2
Bahrain	43.8	19.8	269 (231-312)	35.5 (25.6-49.2)	2.3 (1.5-3.4)	13.2	0.9
Cyprus	12.7	11.5	627 (593-663)	37.0 (24.7-55.9)	10.4 (4.5-14.4)	5.9	1.7
Egypt	39.8	30.9	572 (483-673)	83.2 (59.4-118.1)	7.5 (4.9-11.5)	14.6	1.3
Iran	21.3	9.0	461(450-471)	38.8 (28.0-54.4)	7.0 (5.4-9.1)	8.4	1.5
Iraq	62.0	13.6	480 (404-569)	67.8 (47.2-98.9)	2.5 (1.7-3.6)	14.1	0.5
Israel	20.2	17.2	502 (493-510)	30.3 (22.1-41.8)	7.4 (5.3-10.3)	6.0	1.5
Kuwait	89.4	16.6	218 (195-242)	34.8 (27.8-43.9)	3.5 (2.5-4.9)	15.9	1.6
Lebanon	19.2	16.9	659 (601-722)	60.1 (39.1-93.3)	6.5 (4.1-10.2)	9.1	1.0
Oman	39.9	9.6	291 (276-307)	40.9 (29.5-57.3)	3.5 (2.6-4.8)	14.1	1.2
Qatar	52.6	20.2	148 (120-182)	18.1 (12.5-26.4)	0.9 (0.5-1.4)	12.2	0.6
Saudi Arabia	48.6	13.6	356 (299-428)	47.3 (34.2-65.9)	5.2 (3.6-7.4)	13.3	1.4
Syria	23.1	14.1	737 (629-870)	59.5 (38.3-93.2)	7.0 (4.5-11.0)	8.1	0.9
UAE	59.7	16.4	282 (217-361)	32.3 (20.7-50.5)	6.3 (4.1-9.6)	11.5	2.2
Yemen	37.4	14.7	574 (486-684)	56.8 (34.5-98.0)	6.4 (4.1-9.9)	9.9	1.1

PM_{2.5}* represents country-level and population weighted PM_{2.5}. All-cause mortality statistics (pre-COVID) were obtained from the GBD for 2017 (<http://ghdx.healthdata>)³³. Reported PM_{2.5} excess mortality is due to total (natural and anthropogenic) PM_{2.5}.

Fig. S9). The biomass-burning BC component is rather constant along the ship route and accounts for about 20%–40% of the total BC. The fossil fuel BC component contributes the remaining 60%–80%, but this proportion is enhanced near the pollution centers, especially over the Arabian Gulf, suggestive of a contribution from the petroleum industry.

By scaling the BC emissions from the flaring activity by a factor of thirty⁵¹, we derived optimal BC results that minimize the bias over the Arabian Gulf (Supplementary Fig. S8). Our calculations show that the baseline speciated BC emissions account for 0.54 Tg year⁻¹ domain-wide. The non-speciated PM_{2.5} emissions (PM_{2.5}-OC-BC) contribute additional 1.14 Tg year⁻¹ or 213%. The recovered source of emissions (scaled flaring emissions) adds another 0.97 Tg year⁻¹ or 58%. While the flaring activity itself is unlikely to fully explain the missing source, it coincides spatially with the backward trajectories and allows us to restrict the location to the Mesopotamia region. The combined comparison of the O₃, RO₂, VOC, BC and sulfate over the Arabian Gulf further indicates that the missing source is petrochemical in nature.

Health effects of ambient air pollution. Figure 2c presents the submicron size fraction of PM in the Middle East and Fig. 4 shows the accompanying PM_{2.5} levels. Table 1 lists the annual mean exposure to PM_{2.5} in 14 countries. We find that the submicron PM is nearly entirely anthropogenic, whereas this varies between 20% and 80% for PM_{2.5} due to a larger contribution by mineral dust. In Egypt (population 102 million) this fraction is ~78%, while in Saudi Arabia (population 35 million) this fraction is 28%. To estimate the chronic health outcomes from air pollution, the model results for annual mean PM_{2.5} have been applied in the recent MR-BRT (meta-regression—Bayesian, regularized, trimmed) exposure (dose) response relationships, following the approach of the Global Burden of Disease (GBD) studies^{33,34,52}.

The MR-BRT functions include cause-specific risk expressions for ischemic heart disease, stroke (ischemic and hemorrhagic), chronic obstructive pulmonary disease, lung cancer and type-II diabetes among adults (population with age >25 years), acute lower respiratory tract infection among children (population under the age of 5). This yields age-dependent hazard ratios R(z), where z represents the annual mean concentration, from which the attributable fraction is computed: AF = [R(z) - 1] / R(z). The excess mortality ΔM follows from the expression ΔM = BMR × AF × P, in which the BMR is the baseline mortality rate and P the population that is exposed. The results in Table 1 include the 95% confidence intervals, which have been estimated by accounting for the uncertainties in BMRs obtained from the GBD and those for the MR-BRT splines used to obtain hazard ratios²⁷.

The health outcomes from the exposure to O₃ are based on hazard ratios for respiratory disease, using the expression R(z) = exp^{βΔx}, in which Δx = max [0, (O₃ - LCC)], using the coefficients from ref. ⁵³. We calculated β through ln-R(z) of 1.12 (with a 95% confidence interval of 1.08 - 1.16 for a 10 ppbv increase in O₃, adjusted for near-source PM_{2.5}, regional PM_{2.5} and NO₂). The β obtained was then used to derive the R(z) for exposure to O₃ using two low-concentration cut-offs (LCCs: 26.7 ppb and 31.1 ppb). For details and discussion about methods and statistical uncertainties we refer to ref. ^{32,34,52}.

Data availability

The data used in this study are archived and distributed through the KEEPER service of the Max Planck Digital Library (<https://keeper.mpg.de/group/1235/>, last access: 18

July 2022) and have been freely available from August 2019 to all scientists agreeing to the AQABA protocol. The model output is available online at <https://keeper.mpg.de/d/0b2243fd17d942048083/> (last access: 18 July 2022).

Code availability

The WRF-Chem model is developed by the community collaboratively under the leadership of the NOAA/ESRL scientists. The model is publicly available at <https://github.com/wrf-model/WRF>.

Received: 9 February 2022; Accepted: 3 August 2022;

Published online: 22 September 2022

References

- Osipov, S., Stenchikov, G., Brindley, H. & Banks, J. Diurnal cycle of the dust instantaneous direct radiative forcing over the Arabian Peninsula. *Atmos. Chem. Phys.* **15**, 9537–9553 (2015).
- Almazroui, M. & Hasanean, H. M. Saudi Arabia's summer surface air temperature and its association with circulation patterns. *Int. J. Climatol.* **40**, 5727–5743 (2020).
- Ukhov, A. et al. Assessment of natural and anthropogenic aerosol air pollution in the Middle East using MERRA-2, CAMS data assimilation products, and high-resolution WRF-Chem model simulations. *Atmos. Chem. Phys.* **20**, 9281–9310 (2020).
- Jish Prakash, P., Stenchikov, G., Kalenderski, S., Osipov, S. & Bangalath, H. The impact of dust storms on the Arabian Peninsula and the Red Sea. *Atmos. Chem. Phys.* **15**, 199–222 (2015).
- Kok, J. F. et al. Smaller desert dust cooling effect estimated from analysis of dust size and abundance. *Nat. Geosci.* **10**, 274–278 (2017).
- Brindley, H. et al. An assessment of the quality of aerosol retrievals over the Red Sea and evaluation of the climatological cloud-free dust direct radiative effect in the region. *J. Geophys. Res.: Atmos.* **120**, 810–862 (2015).
- McLinden, C. A. et al. Space-based detection of missing sulfur dioxide sources of global air pollution. *Nat. Geosci.* **9**, 496–500 (2016).
- Fioletov, V. et al. Anthropogenic and volcanic point source SO₂ emissions derived from TROPOMI on board Sentinel-5 Precursor: First results. *Atmos. Chem. Phys.* **20**, 5591–5607 (2020).
- Friedlingstein, P. et al. Global Carbon Budget 2020. *Earth Syst. Sci. Data* **12**, 3269–3340 (2020).
- Lelieveld, J. et al. Severe ozone air pollution in the Persian Gulf region. *Atmos. Chem. Phys.* **9**, 1393–1406 (2009).
- Ukhov, A. et al. Study of SO₂ Pollution in the Middle East Using MERRA-2, CAMS Data Assimilation Products, and High-Resolution WRF-Chem Simulations. *J. Geophys. Res.: Atmos.* **125**, e2019JD031993 (2020).
- McDuffie, E. E. et al. Source sector and fuel contributions to ambient PM_{2.5} and attributable mortality across multiple spatial scales. *Nat. Commun.* **12**, 3594 (2021).

13. Pfannerstill, E. Y. et al. Shipborne measurements of total OH reactivity around the Arabian Peninsula and its role in ozone chemistry. *Atmos. Chem. Phys.* **19**, 11501–11523 (2019).
14. Bourtsoukidis, E. et al. Non-methane hydrocarbon (C2-C8) sources and sinks around the Arabian Peninsula. *Atmos. Chem. Phys.* **19**, 7209–7232 (2019).
15. Tadic, I. et al. Net ozone production and its relationship to nitrogen oxides and volatile organic compounds in the marine boundary layer around the Arabian Peninsula. *Atmos. Chem. Phys.* **20**, 6769–6787 (2020).
16. Celik, S. et al. Influence of vessel characteristics and atmospheric processes on the gas and particle phase of ship emission plumes: In situ measurements in the Mediterranean Sea and around the Arabian Peninsula. *Atmos. Chem. Phys.* **20**, 4713–4734 (2020).
17. Paris, J. D. et al. Shipborne measurements of methane and carbon dioxide in the Middle East and Mediterranean areas and the contribution from oil and gas emissions. *Atmos. Chem. Phys.* **21**, 12443–12462 (2021).
18. Dayan, U., Ricaud, P., Zbinden, R. & Dulac, F. Atmospheric pollution over the eastern Mediterranean during summer—a review. *Atmos. Chem. Phys.* **17**, 13233–13263 (2017).
19. Lelieveld, J. et al. Global air pollution crossroads over the Mediterranean. *Science* **298**, 794–799 (2002). no. 5594.
20. van Damme, M. et al. Industrial and agricultural ammonia point sources exposed. *Nature* **564**, 99–103 (2018).
21. Liu, F. et al. A new global anthropogenic SO₂ emission inventory for the last decade: A mosaic of satellite-derived and bottom-up emissions. *Atmos. Chem. Phys.* **18**, 16571–16586 (2018).
22. World Health Organization, WHO global air quality guidelines. *WHO, Geneva* (2021).
23. Percival, C. J. et al. Regional and global impacts of Criegee intermediates on atmospheric sulphuric acid concentrations and first steps of aerosol formation. *Faraday Discuss.* **165**, 45–73 (2013).
24. Dovrou, E. et al. Towards a chemical mechanism of the oxidation of aqueous sulfur dioxide via isoprene hydroxyl hydroperoxides (ISOPOOH). *Atmos. Chem. Phys.* **21**, 8999–9008 (2021).
25. Moffet, R. C. & Prather, K. A. In-situ measurements of the mixing state and optical properties of soot with implications for radiative forcing estimates. *Proc. Natl. Acad. Sci. USA* **106**, 11872–11877 (2009).
26. Fierce, L. et al. Radiative absorption enhancements by black carbon controlled by particle-to-particle heterogeneity in composition. *Proc. Natl. Acad. Sci. USA* **117**, 5196–5203 (2020).
27. Bates, J. T. et al. Review of acellular assays of ambient particulate matter oxidative potential: Methods and relationships with composition, sources, and health effects. *Environ. Sci. Technol.* **53**, 4003–4019 (2019).
28. Conrad, B. M. & Johnson, M. R. Field measurements of black carbon yields from gas flaring. *Environ. Sci. Technol.* **51**, 1893–1900 (2017).
29. Ginoux, P. et al. Sources and distributions of dust aerosols simulated with the GOCART model. *J. Geophys. Res.* **106**, 20255–20273 (2001).
30. Kok, J. F. A scaling theory for the size distribution of emitted dust aerosols suggests climate models underestimate the size of the global dust cycle. *Proc. Natl. Acad. Sci. USA* **108**, 1016–1021 (2011).
31. Karydis, V. A., Tsimpidi, A. P., Pozzer, A., Astitha, M. & Lelieveld, J. Effects of mineral dust on global atmospheric nitrate concentrations. *Atmos. Chem. Phys.* **16**, 1491–1509 (2016).
32. Chowdhury, S., Pozzer, A., Dey, S., Klingmueller, K. & Lelieveld, J. Changing risk factors that contribute to premature mortality from ambient air pollution between 2000 and 2015. *Environ. Res. Lett.* **15**, 074010 (2020).
33. Abbafati, C. et al. Global burden of 87 risk factors in 204 countries and territories, 1990–2019: a systematic analysis for the Global Burden of Disease Study 2019. *Lancet* **396**, 1223–1249 (2020).
34. Chowdhury, S. et al. Global health burden of ambient PM 2.5 and the contribution of anthropogenic black carbon and organic aerosols. *Environ. Int.* **159**, 107020 (2022).
35. Clegg, S. L. & Brimblecombe, P. Solubility of ammonia in pure aqueous and multicomponent solutions. *J. Phys. Chem.* **93**, 7237–7248 (2002).
36. Powers, J. G. et al. The Weather Research and Forecasting model: Overview, system efforts, and future directions. *Bull. Am. Meteorol. Society* **98**, 1717–1737 (2017).
37. Fast, J. D. et al. Evolution of ozone, particulates, and aerosol direct radiative forcing in the vicinity of Houston using a fully coupled meteorology-chemistry-aerosol model. *J. Geophys. Res.: Atmos.* **111**, 15 (2006).
38. Ahmadov, R. et al. A volatility basis set model for summertime secondary organic aerosols over the eastern United States in 2006. *J. Geophys. Res.: Atmos.* **117**, n/a–n/a (2012).
39. Stockwell, W. R., Kirchner, F., Kuhn, M. & Seefeld, S. A new mechanism for regional atmospheric chemistry modeling. *J. Geophys. Res. Atmos.* **102**, 847–872 (1997).
40. Ackermann, I. J. et al. Modal aerosol dynamics model for Europe: Development and first applications. *Atmos. Environ.* **32**, 2981–2999 (1998).
41. Fountoukis, C. & Nenes, A. ISORROPIAII: A computationally efficient thermodynamic equilibrium model for K⁺-Ca²⁺-Mg²⁺-NH₄⁺-Na⁺-SO₄²⁻-SO₄²⁻-SO₄²⁻-H₂O aerosols. *Atmos. Chem. Phys.* **7**, 4639–4659 (2007).
42. Gelaro, R. et al. The modern-era retrospective analysis for research and applications, version 2 (MERRA-2). *J. Clim.* **30**, 5419–5454 (2017).
43. Guevara, M., Tena, C., Porquet, M. & Jorba, O. & Pérez García-Pando, C. HERMESv3, a stand-alone multi-scale atmospheric emission modelling framework-Part 1: Global and regional module. *Geosci. Model Dev.* **12**, 1885–1907 (2019).
44. Johansson, L., Jalkanen, J. P. & Kukkonen, J. Global assessment of shipping emissions in 2015 on a high spatial and temporal resolution. *Atmos. Environ.* **167**, 403–415 (2017).
45. Janssens-Maenhout, G. et al. HTAP_v2.2: a mosaic of regional and global emission grid maps for 2008 and 2010 to study hemispheric transport of air pollution. *Atmos. Chem. Phys.* **15**, 11411–11432 (2015).
46. Crippa, M. et al. High resolution temporal profiles in the Emissions Database for Global Atmospheric Research. *Sci. Data* **7**, 1–17 (2020).
47. Wiedinmyer, C., Yokelson, R. J. & Gullett, B. K. Global emissions of trace gases, particulate matter, and hazardous air pollutants from open burning of domestic waste. *Environ. Sci. Technol.* **48**, 9523–9530 (2014).
48. Kaiser, J. W. et al. Biomass burning emissions estimated with a global fire assimilation system based on observed fire radiative power. *Biogeosciences* **9**, 527–554 (2012).
49. Lelieveld, J. et al. The South Asian monsoon—pollution pump and purifier. *Science* **361**, 270–273 (2018).
50. Zotter, P. et al. Evaluation of the absorption Ångström exponents for traffic and wood burning in the Aethalometer-based source apportionment using radiocarbon measurements of ambient aerosol. *Atmos. Chem. Phys.* **17**, 4229–4249 (2017).
51. Caseiro, A., Gehrke, B., Rücker, G., Leimbach, D. & Kaiser, J. W. Gas flaring activity and black carbon emissions in 2017 derived from the Sentinel-3A Sea and Land Surface Temperature Radiometer. *Earth Syst. Sci. Data* **12**, 2137–2155 (2020).
52. Lelieveld, J. et al. Loss of life expectancy from air pollution compared to other risk factors: a worldwide perspective. *Cardio. Res.* **116**, 1910–1917 (2020).
53. Turner, M. C. et al. Long-Term Ozone Exposure and Mortality in a Large Prospective Study. *Am. J. Resp. Critical Care Med.* **193**, 1134–1142 (2016).

Acknowledgements

We thank James Brooks and Eoghan Darbyshire of the University of Manchester, UK, for their help with the aerosol mass spectrometry measurements. We thank Ravan Ahmadov and Jordan Schnell of the University of Colorado, USA, for sharing and coupling the new TUV scheme with the MADE_VBS in WRF-Chem. We acknowledge the Max Planck Society for funding the AQABA campaign.

Author contributions

S.O. conducted the model simulations and analyzed the results. S.C. conducted the excess mortality calculations. S.O. and J.L. drafted the article. J.C., I.T., F.D., S.B., P.E., F.F., H.F., H.H., M.P., P.V., J.S., J.W. performed the measurements. J.L., G.S., A.U., A.P., M.F. and E.P. contributed to the analyses, and A.U., A.P. to model development. All authors contributed to the writing of the article.

Funding

Open Access funding enabled and organized by Projekt DEAL.

Competing interests

The authors declare no competing interests.

Additional information

Supplementary information The online version contains supplementary material available at <https://doi.org/10.1038/s43247-022-00514-6>.

Correspondence and requests for materials should be addressed to Jos Lelieveld.

Peer review information *Communications Earth & Environment* thanks the anonymous reviewers for their contribution to the peer review of this work. Primary Handling Editors: Clare Davis. Peer reviewer reports are available.

Reprints and permission information is available at <http://www.nature.com/reprints>

Publisher's note Springer Nature remains neutral with regard to jurisdictional claims in published maps and institutional affiliations.



Open Access This article is licensed under a Creative Commons Attribution 4.0 International License, which permits use, sharing, adaptation, distribution and reproduction in any medium or format, as long as you give appropriate credit to the original author(s) and the source, provide a link to the Creative Commons license, and indicate if changes were made. The images or other third party material in this article are included in the article's Creative Commons license, unless indicated otherwise in a credit line to the material. If material is not included in the article's Creative Commons license and your intended use is not permitted by statutory regulation or exceeds the permitted use, you will need to obtain permission directly from the copyright holder. To view a copy of this license, visit <http://creativecommons.org/licenses/by/4.0/>.

© The Author(s) 2022